Physics of Fluids

RESEARCH ARTICLE | MARCH 06 2024

Experimental and numerical investigation of droplet–fiber interaction on mechanically excited fiber

A. Schwarzwaelder ; F. Freese ; J. Meyer ; K. Loganathan ; H. Tietze ; A. Dittler ; U. Janoske

Physics of Fluids 36, 032006 (2024)
https://doi.org/10.1063/5.0188784

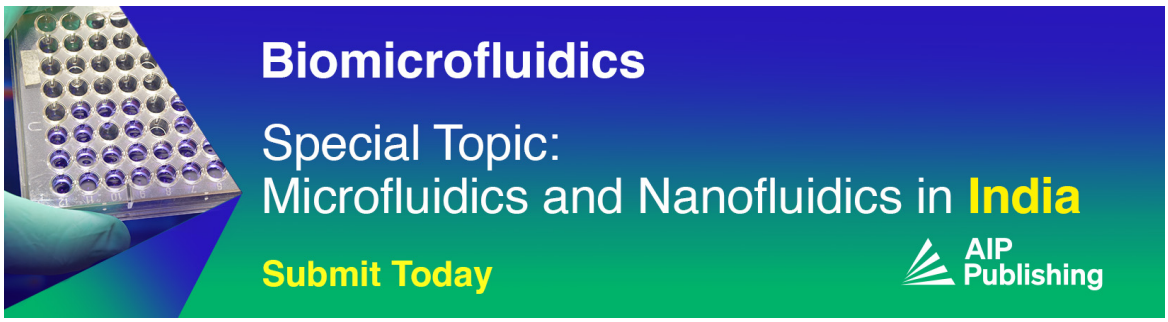

Experimental and numerical investigation of droplet–fiber interaction on mechanically excited fiber

Cite as: Phys. Fluids **36**, 032006 (2024); doi: 10.1063/5.0188784
Submitted: 23 November 2023 · Accepted: 15 February 2024 ·
Published Online: 6 March 2024

A. Schwarzwaelder,[1,a)] F. Freese,[2,b)] J. Meyer,[1,c)] K. Loganathan,[2,d)] H. Tietze,[1,e)] A. Dittler,[1,f)] and U. Janoske[2,g)]

AFFILIATIONS

[1]Institute of Mechanical Process Engineering and Mechanics, Karlsruhe Institute of Technology, 76131 Karlsruhe, Germany
[2]Chair of Fluid Mechanics, University of Wuppertal, 42119 Wuppertal, Germany

[a)]**Author to whom correspondence should be addressed:** alexander.schwarzwaelder@kit.edu
[b)]**Electronic mail:** freese@uni-wuppertal.de
[c)]**Electronic mail:** joerg.meyer@kit.edu
[d)]**Electronic mail:** kamalesh.loganathan@uni-wuppertal.de
[e)]**Electronic mail:** hannah.tietze@alumni.kit.edu
[f)]**Electronic mail:** achim.dittler@kit.edu
[g)]**Electronic mail:** uwe.janoske@uni-wuppertal.de

ABSTRACT

In this study, for the first time, the droplet–fiber interaction on a mechanically excited fiber is examined in the direction of the fiber axis. Highly spatially and temporally resolved simulations and experimental investigations provide information on the relative position of the center of the projected area of the droplet and the center of the fiber, the relative angular position, and the deformation of the droplet using a skeleton line. To attain this, a state-of-the-art camera technology was employed in the experiments, while the volume of fluid method was utilized for the modeling of the multi-phase flow. Additionally, an overset method for the movement of the fiber was applied in the computational fluid dynamics simulations. Characteristic motion patterns, whether occurring in isolation, in sequence, or superimposed, are identified, representing a prerequisite for the detachment of the droplet from the fiber. Despite the simplified assumption of a two-dimensional simulation, the motion patterns observed in the simulation are in good agreement with the experimental data. The obtained results contribute to a fundamental understanding of the mechanisms responsible for the detachment of a droplet in the context of the droplet–fiber interaction within the excited coalescence filters.

I. INTRODUCTION

The interaction between droplets and fibers plays a key role in a wide range of industrial applications,[1,2] especially in coalescence filtration.[3,4] Here, fibrous filter materials are used to filter tiny droplets, such as oil droplets from oil mist. Typically, glass and synthetic fibers are used.

Reducing a coalescence separator to its core element, a single collector fiber allows for *in situ* measurements of fundamental droplet–fiber interactions using optical imaging methods. Optical accessibility into a fibrous material is missing in a practical coalescence filter, thus precluding this possibility. It should be noted that while this simplified approach allows for consideration of fundamental processes involved in fiber–droplet interaction, it fails to account for crucial processes like channel formation or oil sail formation.[3]

There is extensive research in the literature on the interaction between droplets and fibers. These studies investigate the detachment of individual droplets from a fiber,[5] the transport of droplets along a fiber, the separation of droplets from mist,[6] and the determination of contact angles on fibers.[7]

Investigations of droplet–fiber interactions have primarily focused on static fibers. In certain applications, filters are subjected to vibration caused by external forces from wind or vibrating devices.[8–10]

To enhance the separation of water and diesel in water-diesel-separation, Yang *et al.*[8] examined the effect of vibrations on removing water droplets from the upstream surface of the fiber mats. The findings demonstrate that vibration enhanced the separation efficiency, subject to the filter's orientation to gravity and vibrational frequencies.

Crucial research on the interaction between fiber and droplets in vibrating circumstances was conducted by Poulain and Carlson.[11]

Poulain and Carlson[11] utilized an inclined nylon fiber in their study. Their research focused on the change of the contact angle between the droplet and the fiber during sliding along the fiber, depending on the mechanical excitation of the fiber. Furthermore, they outlined different regimes of the droplet motion based on excitation parameters (amplitude and frequency). These regimes are categorized as harmonic pumping, subharmonic pumping, oscillation, and rocking. Pumping describes the deformation where the droplet periodically stretches and flattens at the same frequency as the excitation frequency of the fiber. Subharmonic pumping refers to the droplet deformation at half of the excitation frequency. Swinging describes a movement of the droplet in the circumferential direction of the fiber, while rocking describes a droplet deformation in the axial direction of the fiber. In their case, rocking only occurs in the case of an inclined fiber and the excitation component achieved in the fiber axis direction. Even though their work could contribute significantly to the understanding of the droplet–fiber interaction, the detachment behavior under vibrating conditions and thus possible further mechanisms important for coalescence filtration remain unexamined.

To date, previous work on droplet–fiber interaction has utilized a radial view, which does not provide clear information about movement in the circumferential direction. Therefore, the present study employs an axial perspective of observation on the droplet–fiber interaction as proposed by Farhan *et al.*[12] for a droplet on a static fiber.

II. MATERIALS AND EXPERIMENTAL SETUP

In this study, a blank oleophilic stainless steel (1.4301) fiber from *Carl Haas* with a diameter of 80μm was used. The fiber was secured on one side within an epoxy resin block, allowing for observation along the fiber axis direction (see Fig. 1). After conditioning the fiber in a vertical state with a mass of 0.75 kg attached for an extended period, to ensure maximum straightness, a reduction in length was carried out to mitigate over-swinging tendencies.

The droplet was applied to the fiber by discrete droplet dispensing from a piezoelectric nozzle (*micrdrop Technologies MD-K-130*). The *Roto Inject Fluid NDURANCE* from *Atlas Copco* was used as the fluid. The fluid viscosity was measured with a rheometer (MCR501) and determined to 9999 Pa s. The piezoelectric nozzle precisely dispensed individual droplets, each with a volume of 0.22 nl at a frequency of 100 Hz, onto a spot on the resting fiber, so that the final droplet volume of the droplet on the fiber was achieved by coalescence of a defined number of droplets. The oil temperature in the nozzle was set at 80 °C. The nozzle was positioned in relation to the fiber through mounting it on motorized linear axes configured in the *xyz*-plane (refer to Fig. 2).

For the experiments with an excited fiber, four specific droplet volumes were used at four different excitation amplitudes each combined with three specific excitation frequencies (see Table I).

An electrodynamic shaker (*ETS L315M*) is utilized for mechanically exciting the fiber. Four amplitudes (0.05, 0.25, 0.5, and 0.75 mm) were used, and the fiber was excited at frequencies of 540 and 100 Hz

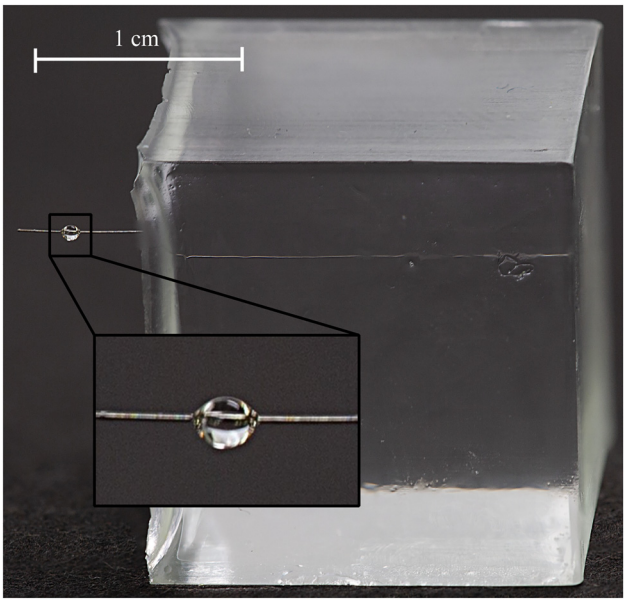

FIG. 1. Fiber in an epoxy resin block.

for each droplet volume. Furthermore, a third frequency was utilized, depending on the respective amplitude at which the shaker is fully utilized. This is 540 Hz for an amplitude of 0.05 mm, 240 Hz at $A = 0.25$mm, 170 Hz at $A = 0.5$mm, and 140 Hz at $A = 0.75$mm. The excitation has always been a sine wave. The shaker ramps up the oscillation up to the specified parameters over a period of 3 s. A high-speed camera (i-speed 721) with a high magnification lens (Navitar Zoom 6000 combined with a 0.67× extension ring) was used in the

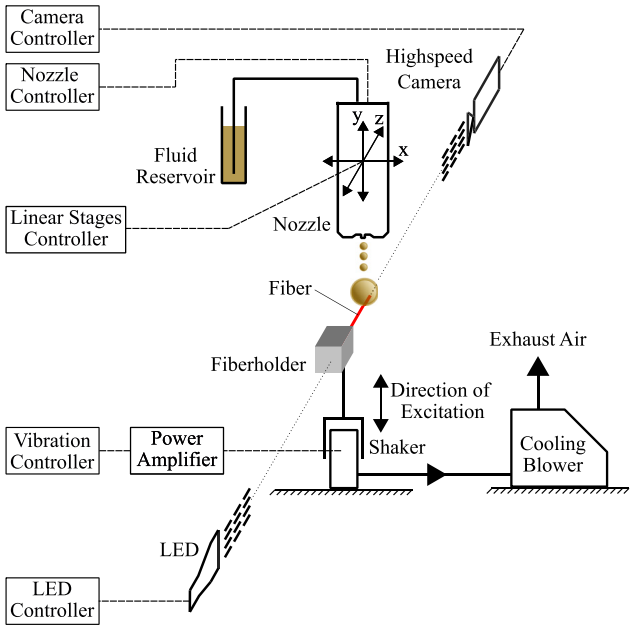

FIG. 2. Schematic diagram of the fiber vibration test system.

TABLE I. Test parameters.

Amplitude A (mm)	0.05, 0.25, 0.5, 0.75
Frequency f (Hz)	40, 100, 540 (0.05 mm), 240 (0.25 mm), 170 (0.5 mm), 140 (0.75 mm)
Droplet volume V (nl)	22, 44, 88, 177

experimental setup. The resulting resolution achieved from the setup is 3.1 μm px^{-1}. A backlight was chosen for the illumination so that the fiber and the droplet to be imaged can be seen as a black surface. The high-speed nature of the imaging necessitates a high intensity for the backlight, which was chosen carefully to ensure that neither the droplet nor the fiber was overexposed and did not appear smaller.

III. METHOD

A. Experimental method

Each of the shown parameter combinations from Table I results in one test and was carried out three times. Each experiment was conducted in the same manner. First, the desired droplet volume was applied to the stationary fiber. Subsequently, an image of the stationary initial state was taken. Then the fiber was excited. Once the droplet was detached due to mechanical excitation or had undergone excitation for 5 s, the camera trigger was activated. As a result, the camera stored the 6 s with 39 877 fps immediately preceding the trigger press. Afterward, the fiber was always removed, cleaned with isopropanol, and then reinstalled on the shaker.

The videos were analyzed using a *MATLAB* script. The evaluation process comprises multiple stages.

First, the position and amplitude of the fiber oscillation are determined by selecting four reference points manually, two at the start of the video and two at the end. This approach was chosen because the fiber can bend slightly due to the one-sided clamping, causing the droplet to experience a greater amplitude than the one specified on the shaker.

Moreover, it is possible for the droplet to detach during the initial ramp-up phase of the oscillation as the amplitude of the shaker increases. Consequently, the amplitude that the droplet experiences at the point of detachment may be less than the specified amplitude.

In the second stage, image post-processing occurs. During this phase, the grayscale image from the camera undergoes binarization using a threshold, whereby all remaining black pixels are connected to a droplet. In the event where there are various black pixel regions, they are divided so that each single black pixel region represents a separate droplet. The resulting droplets are used as input to the *MultiObjectTracker* in *MATLAB*. Tracked droplets are all marked with a yellow boundary box. For each detected droplet, its height, width, center of mass, and skeleton line are determined. Furthermore, each droplet is allocated a *TrackID*, enabling identification of the same object across numerous frames. Refer to Fig. 3 for an illustrative example where all calculated parameters are defined.

B. Numerical method

The overset solver *overInterDyMFoam*, available in the openFOAM® open-source software package distributed by ESI-OpenCFD, version 2206, was employed for simulating the oscillating

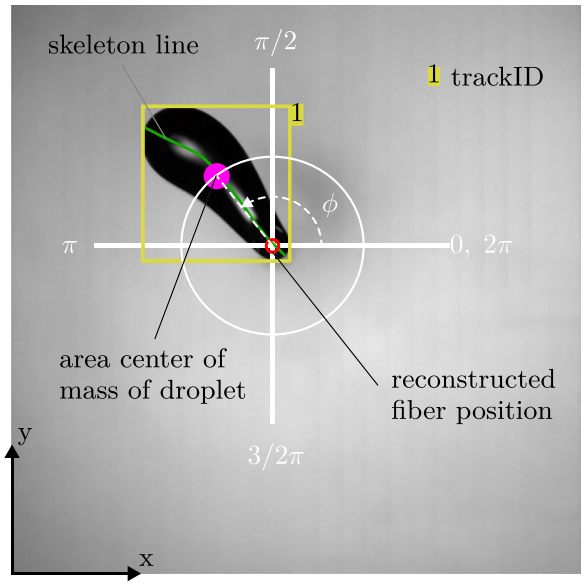

FIG. 3. Post processing.

fiber with the droplet. The overset method establishes connectivity between two or more distinct computational grids through designated interpolation zones. This approach allows the incorporation of body-fitted grids for disparate and independently moving objects within a fluid flow. In addition, fiber movement is orchestrated through a dynamic overset mesh that traverses within a background mesh, and the droplet is simulated using the volume of fluid (VoF) model proposed by Hirt *et al.*[13] This chapter furnishes an overview encompassing the governing equations and the applied overset method.

1. Governing equations

The continuity equation is

$$\vec{\nabla} \cdot \vec{u} = 0, \tag{1}$$

where $\vec{\nabla}$ is the Nabla operator and $\vec{u}$ is the fluid's relative velocity vector,

$$\vec{u} = \vec{u}_0 - \vec{u}_m, \tag{2}$$

using the difference between the absolute velocity $\vec{u}_0$ and the mesh velocity $\vec{u}_m$, which is induced by the displacement of the mesh. Additionally, the momentum equation is denoted as

$$\frac{\partial}{\partial t}(\rho\,\vec{u}) + \vec{\nabla} \cdot (\rho\,\vec{u}\,\vec{u}) = -\vec{\nabla} p_d + \vec{\nabla} \cdot \boldsymbol{\tau} - \vec{g} \cdot \vec{x}\,\vec{\nabla}\rho + \vec{f}_\sigma, \tag{3}$$

where $\vec{g}$ is gravitational acceleration, $\vec{x}$ is the distance vector from a reference position, ρ is the density of the mixture, and $\vec{\nabla}\rho$ is its gradient; the shear-rate tensor

$$\boldsymbol{\tau} = \mu\left[\vec{\nabla}\vec{u} + (\vec{\nabla}\vec{u})^T\right], \tag{4}$$

where μ is the dynamic viscosity of the mixture, $\vec{\nabla}\vec{u}$ is the velocity gradient, $(\vec{\nabla}\vec{u})^T$ is its transpose, $\vec{f}_\sigma$ is the volumetric surface tension

force, and p_d is the reduced pressure. The total pressure can be calculated by

$$p = p_d + \rho \vec{g}\,\vec{x}. \tag{5}$$

The solver *overInterDyMFoam* implements the VoF model for two fluids that can be treated as isothermal, immiscible, and incompressible. The advection of the secondary fluid phase (oil) is governed by

$$\frac{\partial}{\partial t}(\alpha) + \vec{\nabla}\cdot(\alpha\vec{u}) + \vec{\nabla}\cdot\left[\vec{u}_r\,\alpha\,\alpha_p\right] = 0, \tag{6}$$

where α is the volume fraction of the secondary fluid phase, $\alpha_p = 1 - \alpha$ is the volume fraction of the primary fluid phase, and u_r is the relative velocity vector between the two phases active in the interface region of the fluid (for more information about the implementation, refer to Rusche).[14] Additionally, the local density and viscosity are set using the volumetric average of the density of the primary phase ρ_p and secondary phase ρ_s and the viscosity of the primary phase μ_p and secondary phase μ_p,

$$\rho = \alpha\rho_s + \alpha_p\rho_p, \tag{7}$$

$$\mu = \alpha\mu_s + \alpha_p\mu_p. \tag{8}$$

Furthermore, the surface tension force is calculated as a continuum surface force (CSF)[15] by

$$f_\sigma = \sigma\kappa\,\vec{\nabla}\alpha, \tag{9}$$

where σ is the surface tension coefficient, κ is the mean curvature of the free surface, and $\vec{\nabla}\alpha$ is the secondary phase gradient. The curvature in Eq. (9) is calculated using the divergence of the normalized gradient of the secondary phase gradient,

$$\kappa = -\vec{\nabla}\cdot\left(\frac{\vec{\nabla}\alpha}{|\vec{\nabla}\alpha|}\right). \tag{10}$$

2. Model and mesh setup

Figure 4 illustrates the two-dimensional simulation setup referencing the side length of the background mesh $l_{bg} = 20$ mm, the oscillation amplitude A, the diameter of the fiber d_f, the radius of the droplet r_d, and the radius of the overset mesh $r_o = 3.5$ mm. The fiber is initiated in the origin, being entirely immersed in oil, and oscillates in the y-direction. The droplet starts fully concentric around the origin (and the fiber), mirroring the state of the droplet observed in the experiments before oscillation of the fire starts (totally coating the fiber). In the simulation, oil ($\rho = 875\,\mathrm{kg/m^3}$, $\nu = 1.55 \times 10^{-4}\,\mathrm{m^2/s}$, $\sigma = 0.0382\,\mathrm{N/m^2}$) was used for the droplet, and air ($\rho = 1\,\mathrm{kg/m^3}$, $\nu = 1.48 \times 10^{-5}\,\mathrm{m^2/s}$) was used for the surrounding medium. The surface tension coefficient σ was considered constant and measured experimentally. To set the initial phase fraction $\alpha = 1$ for the oil in the two-dimensional simulations, the droplet volume V was used to calculate a sphere volume equivalent radius around the fiber by

$$r_d = \left(\frac{V}{\frac{4}{3}\pi}\right)^{\frac{1}{3}}, \tag{11}$$

knowing that there will be a small error because of the fiber area that is expected to be insignificant.

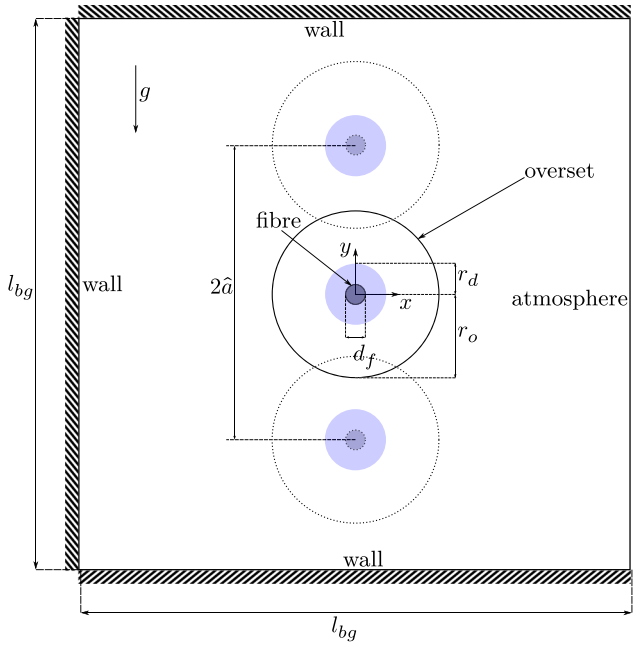

FIG. 4. Simulation setup.

The mesh motion capability of the solver was utilized, so that the fiber together with the overset mesh is moving in the y-direction according to

$$y(t) = A\sin(2\pi f t), \tag{12}$$

where A is the amplitude, f is the frequency, and t is the time. Three of the outer boundaries of the background mesh are declared as static wall, the other side is declared as the outlet with a Dirichlet condition for pressure and a Neumann boundary condition for velocity as stated in Table II. The outer part of the overset mesh is interpolated from the background grid using the inverse distance scheme, the inner boundary of the overset mesh is a wall, moving with the velocity of the overset mesh [calculated utilizing Eq. (12) for mesh displacement].

For the spatial discretization, second-order accurate linear schemes were applied to all gradients and divergence operations except for the diffusive term of the momentum equation, which was discretized using a first-order accurate upwind scheme. All interpolations adopt linear methods, the overset interpolation, specifically, utilizes an inverse distance scheme. In terms of time discretization, a first-order accurate implicit Euler scheme was employed.

TABLE II. Boundary conditions for the overset simulation.

Boundary	Pressure p_d	Velocity u	Oil volume fraction α
Atmosphere	$p_d = 0$	$\frac{\partial\vec{u}}{\partial\vec{n}} = 0$	$\frac{\partial\alpha}{\partial\vec{n}} = 0$
Wall	$\frac{\partial p_d}{\partial\vec{n}} = 0$	$\vec{u} = \vec{0}$	$\frac{\partial\alpha}{\partial\vec{n}} = 0$
Fiber	$\frac{\partial p_d}{\partial\vec{n}} = 0$	$\vec{u} = \vec{u}(t)$	$\frac{\partial\alpha}{\partial\vec{n}} = 0$

In order to keep the Courant number under 0.5, the simulation was performed with a dynamic time step.

Hence, using overset mesh, cell types divide into the three sets:

- Hole cells: cells are masked in the equation and no solution is computed.
- Calculated cells: solution is computed without modification.
- Interpolated cells: to compute cell values, interpolation from one to another mesh is performed. The interpolated cells can be classified as follows:
  - Acceptor cells: they receive their solution by interpolation.
  - Donor cells: they send their solution to their assigned acceptor cells.

To ensure good interpolation quality, the mesh is refined to make sure that the ratio $\frac{V_{ac}}{V_{dc}}$ between the volumes of the acceptor cell V_{ac} and the donor cells V_{dc} does not exceed 5. Due to the unidirectional movement of the overset mesh region through the background mesh, the refinement zone takes on a rectangular shape. This configuration ensures uniform cell refinement along the fiber's trajectory. In total, the mesh is refined six times, once inside an outer interpolation zone and five more times inside inner interpolation zones.

3. Mesh sensitivity analysis

A mesh sensitivity analysis is performed to select the mesh best suited for the simulations. Three different meshes listed in Table III

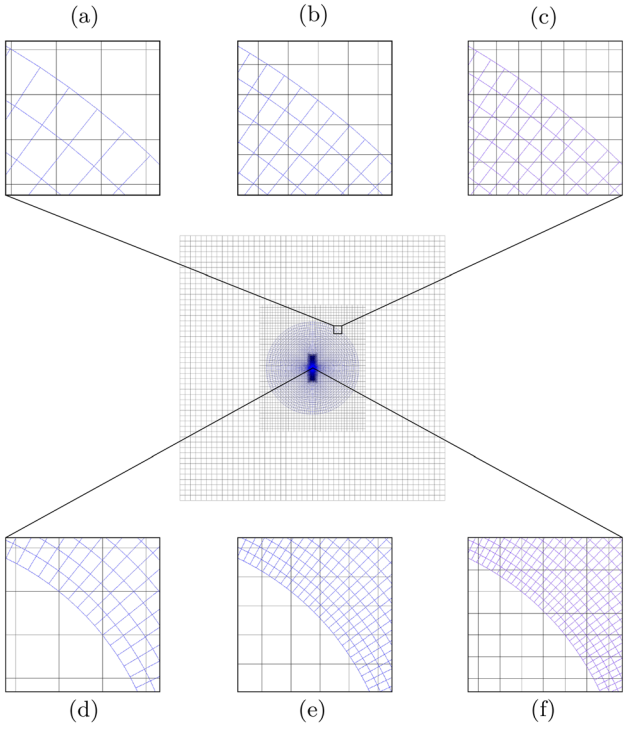

FIG. 5. Coarse mesh in the center with details of the outer overset interpolation zone for the coarse (a), medium (b), and fine grid (c) and the inner overset interpolation zone for the coarse (d), medium (e), and fine (f) grid.

TABLE III. Number of cells in the different grid types for the mesh convergence analysis.

Type	Overset	Background	Total
Coarse	10 500	11 812	22 312
Medium	45 000	48 760	93 760
Fine	150 000	281 872	431 872

where used where each background mesh had the same refinement zones and the default number of cells in background and overset region was multiplied by 1.5 and 2, respectively. Figure 5 depicts the overset coarse mesh in blue and the coarse background mesh in black in the center. The inner and outer interpolation zones of the coarse, medium, and fine mesh are delineated above and below, respectively (Tables II and III).

In order to compare the different meshes with each other, the ratio of the absolute of the relative center of gravity vector

$$|\Delta\vec{C}| = |\vec{C}_D - \vec{C}_F| \tag{13}$$

to the fiber radius r_f is utilized, where $\vec{C}_D$ and $\vec{C}_F$ are the center of gravity of the droplet and fiber, respectively. Figure 6 shows $\frac{|\Delta\vec{C}|}{r_f}$ plotted over the dimensionless time the droplet detaches $\frac{t-t_d}{T}$, employing the detachment time t_d. The mesh sensitivity analysis results indicate that the coarse, medium, and fine meshes produce comparable outcomes, with the droplet requiring a few additional periods to detach from the fiber using the coarse grid. However, the detachment phase remains consistent across all grids. The coarse grid exhibits optimal computational efficiency and is equally accurate in describing the detachment process compared to the other meshes. Consequently, it is chosen for further simulations in this study.

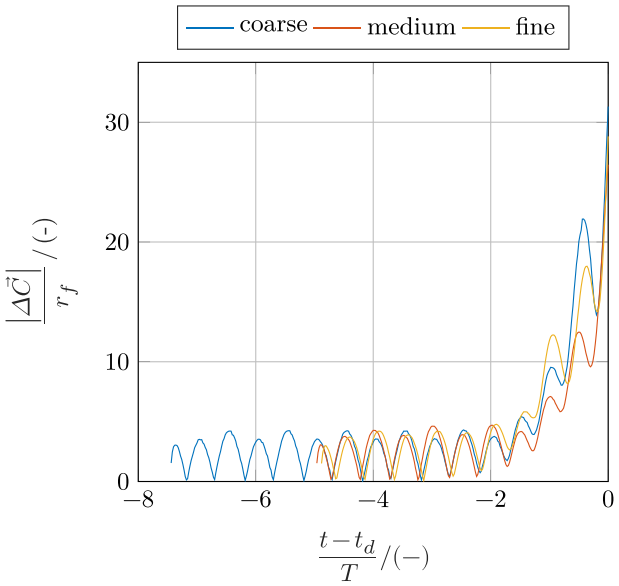

FIG. 6. Results of the mesh independence study.

IV. RESULTS AND DISCUSSION

This chapter presents and discusses results from experiments and simulations on droplet motion patterns. An overview will be provided on observed mechanisms, which consist of either superimposed or consecutive motion patterns resulting in droplet sticking to or detaching from the fiber. The motion patterns are then discussed with exemplary test series using both simulation and experimental data, concluding with a regime map that can aid in predicting droplet behavior in other droplet–fiber systems.

A. Droplet motion patterns

Depending on the excitation parameters, different characteristic motion patterns of the droplets on the fiber could be detected. Four fundamental motion patterns are shown in Fig. 7 with their respective requirements for classification and can be labeled as follows:

1. Quasi-static

A quasi-static behavior of the droplet on the fiber occurs when the center of gravity of the droplet is inside the fiber at any time within a period. To quantify the magnitude of the maximum eccentricity vector of the droplets' center of mass,

$$l_m = \sqrt{l_{m,x}^2 + l_{m,y}^2}$$

is introduced using the eccentricity vector components with the highest magnitude

$$l_{m,x} = \max(|\Delta C_x|), \tag{14}$$

$$l_{m,y} = \max(|\Delta C_y|), \tag{15}$$

with the absolute of the x and y coordinates ($|\Delta C_x|$ and $|\Delta C_x|$) of the eccentricity vector

$$\Delta\vec{C} = \vec{C_D} - \vec{C_F} \tag{16}$$

utilizing the droplets and the fibers' center of mass $\vec{C_D}$ and $\vec{C_F}$, respectively. Finally, the quasi-static behavior is characterized by

$$l_{m,x} < r_F \quad \text{and} \quad l_{m,y} < r_F.$$

2. Vertical oscillation

Vertical oscillation is characterized by a dominant movement in the vertical y-direction of the droplet. The maximum difference in position of the droplet in the y-direction relative to the fiber oscillation must be greater than the fiber diameter and in the x-direction smaller than the fiber diameter within one period,

$$\begin{aligned} &l_{m,x} \geq d_F \quad \text{and} \quad l_{m,y} < d_F, \\ &\Delta\vec{C}_m \,|\, \forall\, \Delta\vec{C} \in S_{\Delta\vec{C}} :\leq |\Delta\vec{C}_m|. \end{aligned} \tag{17}$$

3. Deformation

The deformation of the droplet shape is quantified by the change in the length of the skeleton line. If the length change exceeds 5% within a given time period (here, related to the excitation frequency) starting from any observation time as the start for the period, the droplet change is labeled as deformation. This can be expressed as

$$L_r = \frac{\max(L_{skel})}{\min(L_{skel})} > 1.05.$$

4. Slinging

The slinging motion captures the droplet tendency to rotate around the fiber and is classified by the total angle of the droplets' center of mass $\vec{C_D}$ relative to the center of mass of the fiber $\vec{C_F}$ defined by $\Delta\vec{C}$ rotated around the fiber within the time window of a period's time $\frac{1}{f}$ expressed with

$$\Phi_T = \int_{nT}^{(n+1)T} \frac{\partial}{\partial t}\phi dt \geq \pi.$$

Moreover, to guarantee rotational movement of the droplet around the fiber (rather than erratic oscillations), C_D must be located unambiguously outside of the fiber,

$$l_m > \sqrt{2}\, r_F.$$

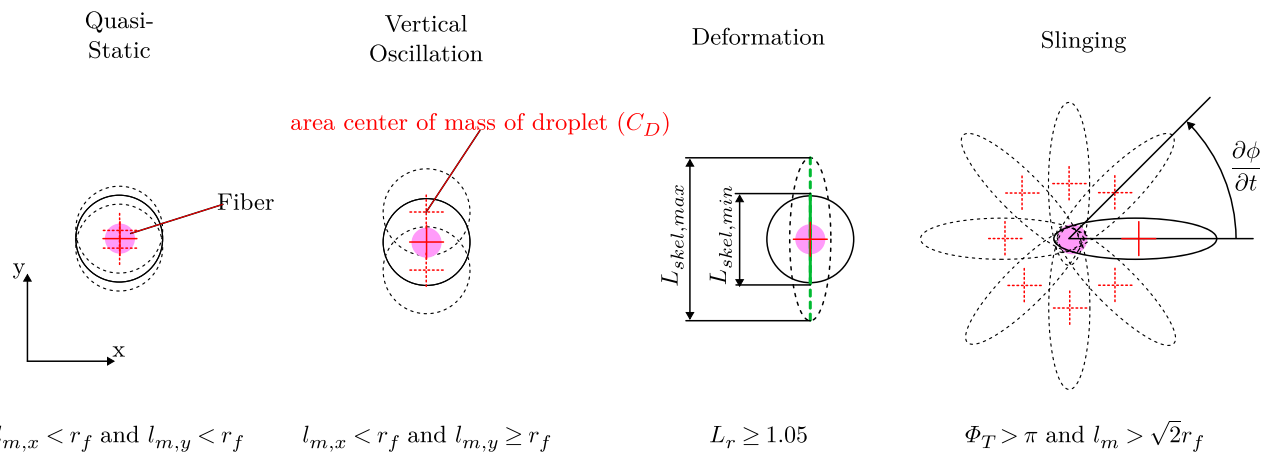

FIG. 7. Motion patterns.

B. Mechanisms

Despite the quasi-static (*) motion pattern, several combinations of characteristic motion patterns result in mechanisms. These motion patterns can be superimposed at the same time or occur one after the other.

Superimposed motion pattern

- Vertical oscillation with deformation
- Slinging with deformation

Consecutive motion patterns

- Vertical oscillation with deformation leading to slinging
- Reoccurring collapsing:
- Vertical oscillation with deformation leading to slinging and followed again by vertical oscillation with deformation

Mechanisms without droplet separation

- Vertical oscillation without deformation (*)
- Vertical oscillation with deformation

Mechanisms leading to droplet separation

- Vertical oscillation with deformation leading to slinging (*)
- Reoccurring collapsing (*)

The mechanisms marked (*) are discussed in more detail. These mechanisms have been selected so that all characteristic motion patterns are covered in detail.

1. Quasi-static

Figure 8 shows a series of raw images from the experiments (blue outline) for a droplet with a volume of $V = 22$ nl excited at a frequency of $f = 100$ Hz and an amplitude of $A = 0.75$ mm. The drop appears black due to the background illumination. As the fiber is cast in an epoxy resin cube, the background illumination causes inhomogeneities in the background of the image. The raw images from the simulation (orange outline) show a black area representing the droplet in the alpha phase. The atmosphere is shown in white, as is the fiber in the center of the droplet. The images are shown at a distance of T/8 periods for a full period, starting at 0.0088 s for the experiment and 0.0124 s for the simulation, within the recorded and simulated timelines, respectively. As shown in Fig. 7, a quasi-static behavior of the droplet on the fiber means that the droplet deforms, rotates, and changes its position relative to the fiber only to a negligible extent. This behavior can be seen in the raw images of the experiment and the simulation for one droplet in Fig. 8.

A better understanding of the relative position of the area center of mass of the droplet to the fiber can be derived from the representation in Fig. 9. It shows the distance between the area center of mass of the droplet and fiber for the x- (ΔC_x) and y-directions (ΔC_y) relative to the fiber diameter (d_F) for the entire period under review. The findings are depicted in orange for the simulation results and blue for the experiment results. It can be derived from Fig. 9 that, in the experiment, the distance $l_{m,x,\mathrm{exp}} = 0.01\,\mathrm{mm} < r_F$ and $l_{m,y,\mathrm{exp}} = 0.06\,\mathrm{mm} < r_F$, while in the simulation $l_{m,x,sim} = 0.001\,\mathrm{mm} < r_F$ and $l_{m,y,sim} = 0.06\,\mathrm{mm} < r_F$. Based to this criterion, the droplet motion pattern is quasi-static in both, the experiment and simulation.

In the simulation, the movement runs vertically, while in the experiments, there is movement of the droplet with respect to the fiber in the x-direction. Presumably, this horizontal movement is mainly due to the free-standing fiber end. As the fiber is clamped on one side, it can deflect in any direction in the xy-plane. Moreover, the fiber's tensile manufacturing process leads to the creation of small grooves that can interfere with the droplet's movement relative to the fiber. Although the fiber's surface undergoes thorough cleaning in an ultrasonic bath and rinsing with isopropanol, other surface inhomogeneities cannot be ruled out, which may also impact the relative movement of the droplet to the fiber.

Figure 10(a) illustrates the total difference in angular position between two successive time steps, while Fig. 10(b) shows the sliding integral of the excitation of the area center of mass with respect to the fiber over one period of the excitation. The experiment's results are depicted by the solid lines, whereas the simulation is presented with dashed lines.

The value of Φ in Fig. 10(a) can be greater than 2π. It can be used to determine the number of revolutions the droplet exhibits around the fiber. When there is a change in the direction of rotation of the droplet area's center of mass around the fiber, the sign of the gradient in the diagram in Fig. 10(a) also changes. The gradient of the graph thus provides information on the rotational speed and is used for comparing simulation and experiment. If the area center of mass of the

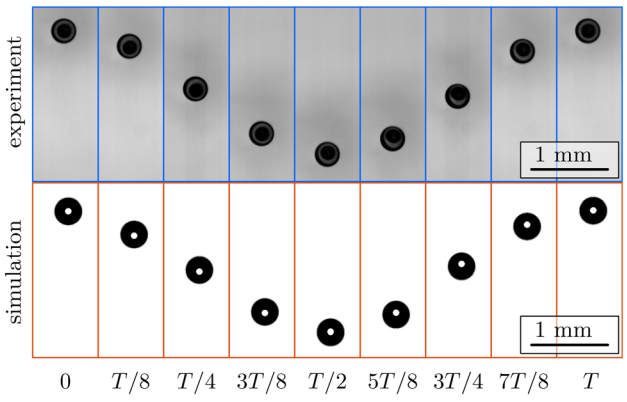

FIG. 8. Raw images taken in the experiment (blue outline) and simulation (orange outline) of a droplet with $V = 22$ nl excited at $f = 100$ Hz and $A = 0.75$ mm.

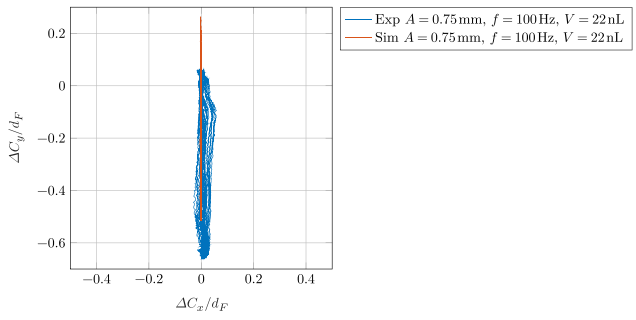

FIG. 9. Relative position for a droplet with $V = 22$ nl excited at $f = 100$ Hz and $A = 0.75$ mm relative to the fiber.

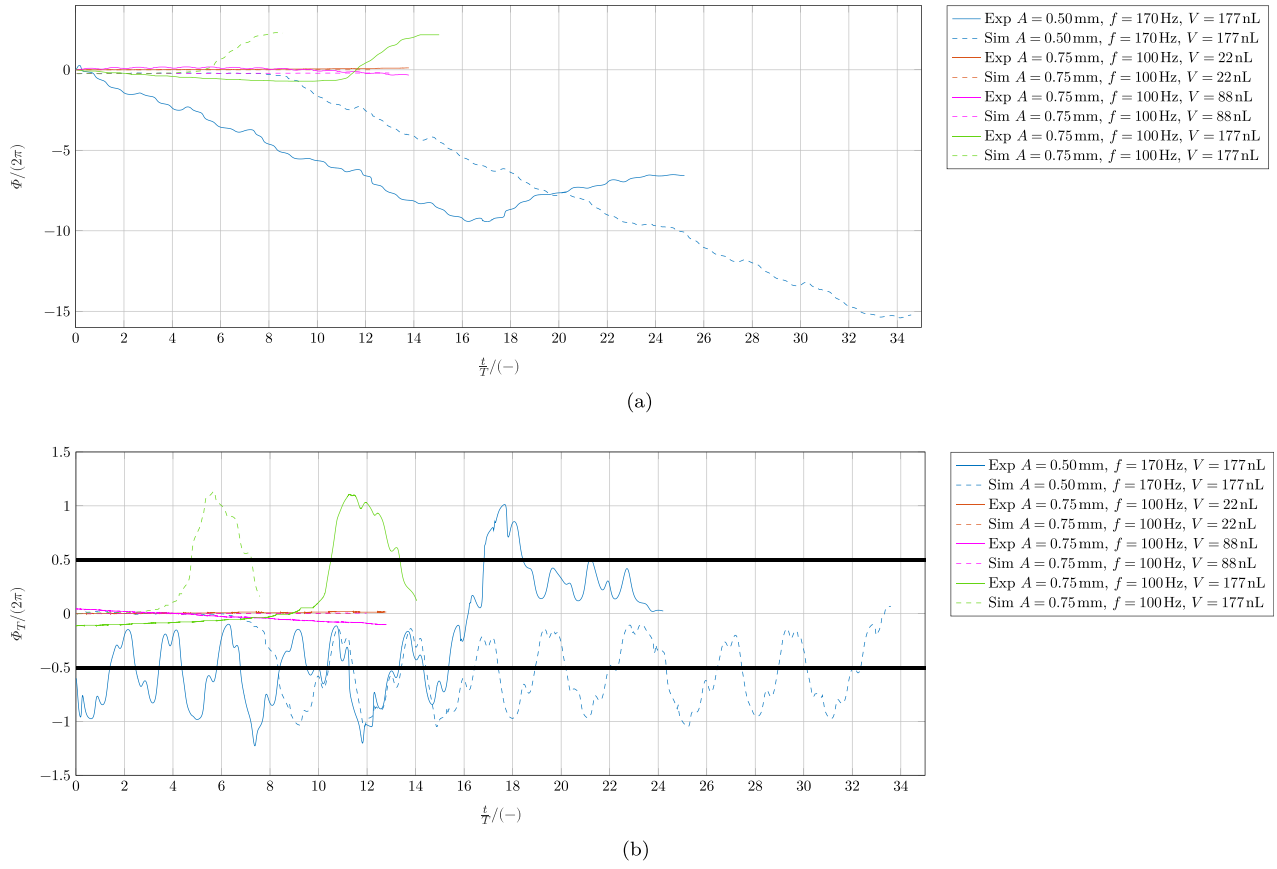

FIG. 10. (a) Angular position ϕ and (b) sliding integral of the angular change with the integration window of one period of excitation Φ_T for four different parameter combinations used in the experiments (continuous line) and simulations (dashed line) relative to the fiber origin; blue: $A = 0.50$ mm, $f = 170$ Hz, $V = 177$ nl; orange: $A = 0.75$ mm, $f = 100$ Hz, $V = 22$ nl; pink: $A = 0.75$ mm, $f = 100$ Hz, $V = 88$ nl; and green: $A = 0.75$ mm, $f = 100$ Hz, $V = 177$ nl.

droplet moves with fluctuating angular velocity around the fiber, this is manifested in Fig. 10(a) by a nonlinear slope.

Figure 10(b), in contrast, displays the change in angular position Φ_T determined by the sliding integral, which has a time span equal to one period of the excitation.

If the droplet rotates around the fiber at exactly the same frequency at which the fiber is excited, then Φ_T must be equal to plus or minus 2π. The sign also indicates the direction of the rotation. A positive sign means that the droplet rotates counterclockwise. If the value is less than or greater than 2π, the droplet rotates around the fiber at a lower or respective higher frequency than the excitation frequency.

If the area center of mass of the droplet moves with fluctuating rotational velocity, indicating fluctuating angular changes over time around the fiber, this is manifested in Fig. 10(b) by local extrema. As mentioned earlier in the mechanisms, a droplet can deform during its rotating motion. The deformation, due to the displacement of the area center of mass radially toward the fiber, influences the rotational velocity. With the help of Fig. 10(b), the cyclic behavior of the deformation can thus be more effectively depicted.

For the discussed case ($A = 0.75$ mm, $f = 100$ Hz, $V = 22$ nl), the sum of the angular change is almost 0 for all time steps where the area center of mass of the droplet is inside the fiber, leading to horizontal components in Fig. 10(a). Fluctuations arise when the droplet area center of mass goes outside the fiber, resulting in an overall increase in Φ up to 0.2π during the entire test duration.

Since the total difference in angular position is small, Φ_T must be close to zero, as shown in Fig. 10(b).

Figure 11 displays the length of the skeleton line throughout the period under consideration relative to the initial value of $L_{skel,0}$. The deformation is negligible for the discussed case (with $A = 0.75$ mm, $f = 100$ Hz, $V = 22$ nl) in both the experiment with $L_{r,\mathrm{exp}} = 0.0159 < 5\%$ as well as in the simulation with $L_{r,sim} = 0.0213 < 5\%$.

2. Vertical oscillation

When the droplet with a volume of 88 nl is excited at a frequency of 100 Hz and an amplitude of 0.075 mm, it adheres almost without deformation and change of position relative to the fiber, as shown in Fig. 12. However, upon closer inspection, it can be observed that there is a slight change in the fiber's position relative to the droplet on the vertical axis.

The relative position of the area center of mass of the droplet to the fiber in Fig. 13 shows in more detail, that the area center of mass of the droplet moves almost on a vertical axis in space similar to the

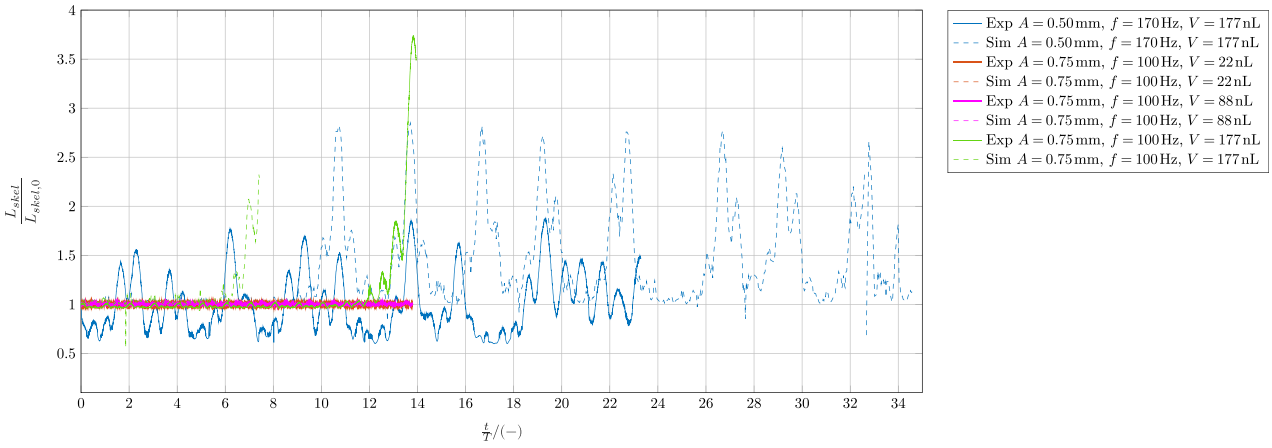

FIG. 11. Deformation of the droplet shown as normalized length of skeleton line for all experiments normalized with the starting value for blue: $L_{skel,\text{exp},0} = 1.25\,\text{mm}$ and $L_{skel,sim,0} = 0.73\,\text{mm}$; orange: $L_{skel,\text{exp},0} = 0.32\,\text{mm}$ and $L_{skel,sim,0} = 0.35\,\text{mm}$; pink: $L_{skel,\text{exp},0} = 0.51\,\text{mm}$ and $L_{skel,sim,0} = 0.58\,\text{mm}$; and green: $L_{skel,\text{exp},0} = 0.68\,\text{mm}$ and $L_{skel,sim,0} = 0.73\,\text{mm}$.

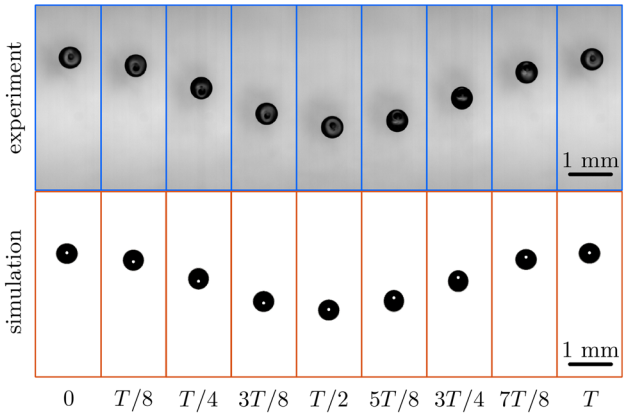

FIG. 12. Raw images of a droplet with $V = 22\,\text{nl}$ excited at $f = 100\,\text{Hz}$ and $A = 0.75\,\text{mm}$.

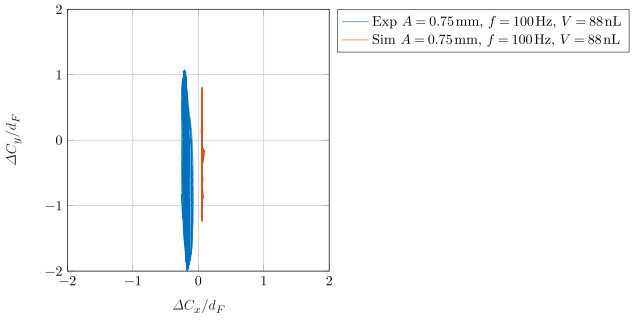

FIG. 13. Relative position of the droplet with $V = 88\,\text{nl}$ excited at $f = 100\,\text{Hz}$ and $A = 0.75\,\text{mm}$ relative to the fiber.

previous considered case in Fig. 9. However, $l_{m,y}$ is now significantly larger compared to the previous discussed example with $l_{m,y,\text{exp}} = 0.24\,\text{mm} > r_F$, while $l_{m,x,\text{exp}}$ is still smaller than the fiber radius with $l_{m,x,\text{exp}} = 0.01\,\text{mm} < r_F$. Therefore, a vertical oscillation is present. The same applies to the simulation with $l_{m,y,sim} = 0.02\,\text{mm}$ and $l_{m,x,sim} = 0.005\,\text{mm}$.

As a result of the droplet's upward movement in relation to the fiber, the simulation yields an almost 0 value for $\Phi_{T,sim}$. Initially, positive values can be seen for $\Phi_{T,\text{exp}}$, which indicates a positive direction of rotation of the droplet around the fiber; negative values are due to a negative direction of rotation. For the experiment, a linear trend with a negative gradient of Φ_T can be recognized approximately. A horizontal linear gradient means that the change in angle over one period cancels out, whereas for a nonzero linear gradient, the net change in angle over one period of excitation remains constant over the test period. This is not a slinging motion around the fiber, but rather a vertical oscillation, as $|\Phi_T| < 2\pi$.

The maximum observed change in length of the skeleton line, as illustrated in Fig. 11, was $L_{r,\text{exp}} = 1.03$ and $L_{r,sim} = 1.047$, indicating a deviation of less than 5%. Hence, according to the previously mentioned categorization, the deformation is negligible.

3. Deformation and slinging

If, at the same frequency ($f = 100\,\text{Hz}$) and amplitude ($A = 0.05\,\text{mm}$) as in the previous experiments, the volume of the droplet is increased to $V = 177\,\text{nl}$, a visible deformation and rotation of the droplet around the fiber is observed. A comparison between the experiment and the simulation reveals similarities in the droplet's movement. At time $T = 0$, the area center of mass of the droplet is almost above the fiber in the first quadrant, resulting from a rotating motion. After $t = T/8$, the droplet is rotated further and is in the second quadrant. As time progresses, the droplet continuously rotates around the fiber until, after a full period of excitation, it has rotated by almost 2π. During this rotating motion, a deformation of the droplet can clearly be observed. The deformation of the fiber amplifies when the droplet is situated on its underside, as seen in Fig. 14.

When plotting $\Delta C_y/d_F$ against $\Delta C_x/d_F$ throughout the test period, a spiral shape is observed, indicating a rotating movement of

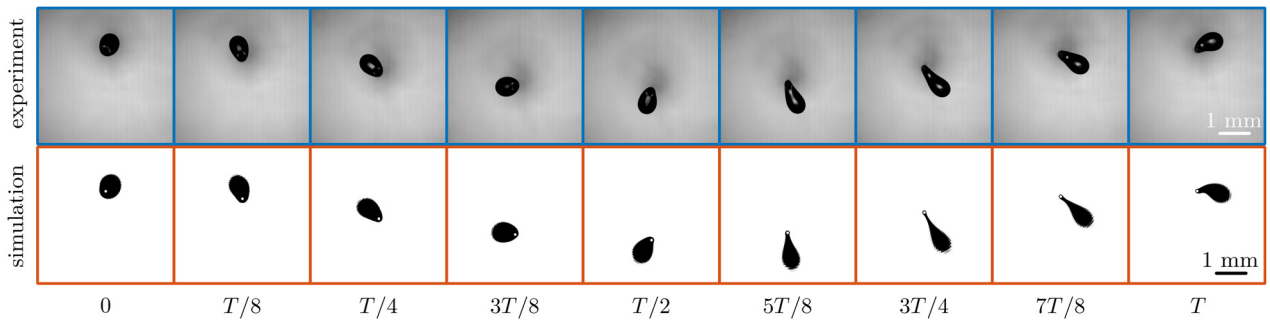

FIG. 14. Raw images of a droplet with $V = 177$ nl excited at $f = 100$ Hz and $A = 0.75$ mm.

the droplet around the fiber. Figure 15 displays all recorded data points until the droplet detachment time. At the onset of both the experiment and simulation, the position of the droplet's area center of mass and that of the fiber are almost identical. Subsequently, the droplet undergoes a vertical oscillation, which changes to a rotational motion. At detachment, the experimental distance l_m is $l_{m,sim}1.04$ mm, while the simulated distance is $l_{m,sim}1.16$ mm, indicating good agreement.

The angular change of the area center of mass of the droplet relative to the fiber origin in Fig. 10(a) shows that the rate of change has a similar magnitude for both the negative and positive angular change. The region demonstrating a negative angle shift is between $0 < t/T < 10$ for the experiment and $0 < t/T < 5$ for the simulation. The region with a negative angle change shows that the total change of $\Phi < |2\pi|$ and, therefore, it can also be concluded that Φ_T is also $2 < \pi$. Therefore, this region does not pertain to slinging, but instead, to vertical oscillation where the droplet does not revolve around the fiber. On the other hand, in the area with a positive gradient for Φ, there is a notably stronger gradient. The values for Φ increase by more than 4π in this region. As Φ_T surpasses π in this range, it results in a slinging and rotating motion of the area center of mass of the droplet around the fiber. Furthermore, it can be stated that for $\Phi_T > 2\pi$, the droplet rotates faster than the excitation frequency, whereas for $\Phi_T < 2\pi$, the rotation takes place at a lower frequency than the excitation frequency, if rotation is present. Additionally, it can be inferred from the change in angle of Φ that the droplet completes at least two complete revolutions around the fiber before detaching. Prior to detachment, the droplet undergoes significant stretching, resulting in a smaller change in angle at the end of Fig. 10(a), which explains the flattened curves.

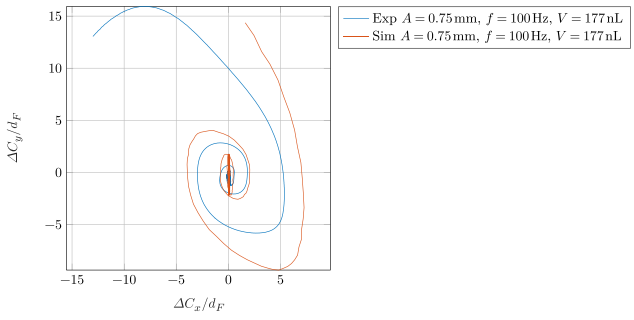

FIG. 15. Relative position of the droplet with $V = 177$ nl excited at $f = 100$ Hz and $A = 0.75$ mm relative to the fiber.

The change in length of the skeleton line again provides information about the deformation of the droplet. Observing Fig. 11, it is evident that rotations around the fiber cause both elongation and subsequent compression of the droplet. Additionally, Fig. 11 illustrates that the amount of compression following elongation is lower and, therefore, the droplet elongates from revolution to revolution. Furthermore, the elongation increase is greater with each revolution. In the experiment, the skeleton line extends by a factor of 3.7 before the detachment of the droplet, whereas the elongation factor in the simulation is 2.8.

4. Reoccurring collapsing

Another characteristic motion pattern can be described as reoccurring collapsing. This occurs when the droplet is stretched initially due to the rotational movement around the fiber. The droplet then bends progressively until it becomes a more compact shape with its area center of mass closer to the fiber. Starting from this state, the droplet resumes rotation and elongation, allowing the described process to repeat itself. The behavior is demonstrated herein for a droplet with a volume of $V = 177$ nl excited at $f = 170$ Hz and $A = 0.5$ mm relative to the fiber (see Fig. 16).

The drop-fiber position mirrors the collapsing behavior, with the area center of mass of the droplet alternating between periods when it is closer to the fiber and periods when it is further away, as shown in Fig. 17. Initially, the behavior seems erratic, but a more detailed examination of the change in the angle of Φ_T in Fig. 10(b) clearly shows a periodic behavior.

The cumulative change in angle Φ demonstrates that, comparable to the previously examined case, the droplet undergoes negligible initial angular change in the experiment. This indicates quasi-static behavior. However, subsequent to $t/T = 9$, the droplet's center of mass with respect to the region is not vertical, which causes the droplet to rotate, eventually leading to reoccurring collapsing. The simulated region is depicted in Fig. 10(a) as an almost linear curve with a negative gradient, with the quasi-static zone being excluded from the simulation. Following excitation, the droplet rotates nearly instantaneously and undergoes reoccurring collapsing. Notably, the direction of the rotational motion reverses at $t/T = 16$, which leads to a positive gradient for Φ_{exp} as opposed to the simulative findings. In the same manner as the temporal progression of Φ_T, the progression of the length of the skeleton line also shows a periodic behavior with a lower frequency than the excitation frequency.

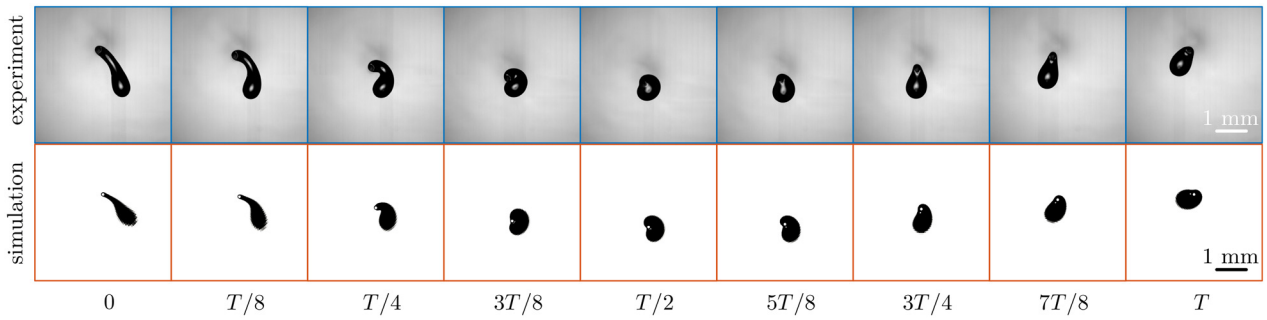

FIG. 16. Raw images of a droplet with $V = 177$ nl excited at $f = 170$ Hz and $A = 0.5$ mm.

Although the droplet detaches in the experiment under the chosen parameters, it does not detach during the simulation. The flattening of Φ_{exp} is caused by the droplet detachment. However, the flattening of Φ_{sim} is due to a more compact droplet on the fiber at this stage.

V. DISCUSSION

In this section, the limits of the two-dimensional simulation is discussed with a focus on the assumption of a constant alpha phase [Eq. (11)].

As depicted in Fig. 18, in the experiments observed, the projected area of the droplet A_e normalized by its projected area in the first image $A_{e,0}$ is not constant for two scenarios (deformation and swinging and reoccurring collapsing). The data are plotted over the dimensionless time $\frac{t}{T}$ and shown until droplet detachment occurs.

This difference between the simulated alpha phase and, respectively, the observed projected droplet area is thought to be one reason for the difference in the length of the skeleton line L_{sekl} between the simulations and the experiments in Fig. 11. An increase in the droplet's projected area in the experiments results from a decrease in the wetted area caused by the elongation of the droplet. The two-dimensional assumption does not hold here. This is also the expected reason for the difference in Fig. 15

This discrepancy is anticipated to disappear if the simulations were conducted in three dimensions. However, introducing three dimensions leads to additional issues such as line contact angle hysteresis and its impact on droplet shape, which complicates the matter.

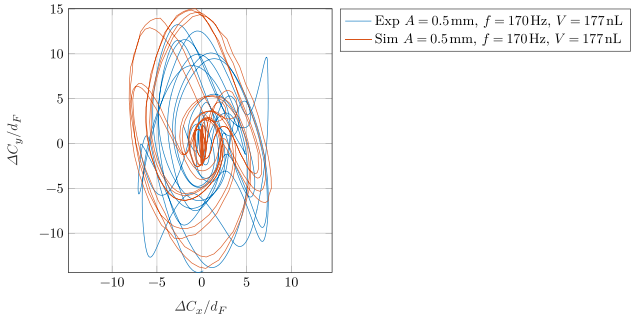

FIG. 17. Relative position of the droplet with $V = 177$ nl excited at $f = 170$ Hz and $A = 0.5$ mm relative to the fiber.

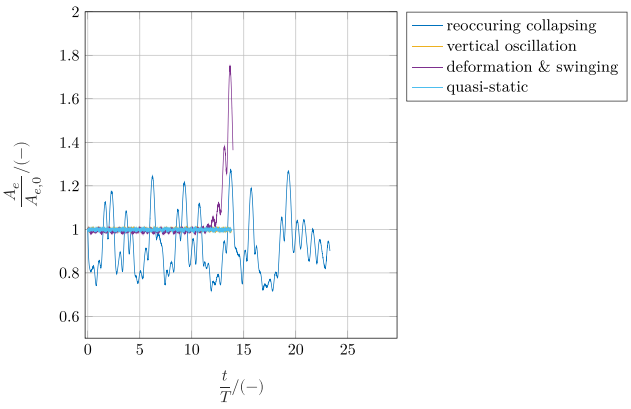

FIG. 18. Relative droplet area measured in the experiments.

This, along with the significant computational expenses, is why the simulations are limited to two dimensions.

VI. DETACHMENT AND STICKING

In filtration applications, the behavior of deposited droplets is essential. Therefore, the knowledge about sticking or detaching droplets is of utmost interest.[16–18] The detachment can occur for different motion patterns shown in Sec. IV. Therefore, in this section, a characterization of these two different states is presented as a function of dimensionless parameters. In Fig. 19, a regime map is presented, where the regimes of detachment and sticking are shown as dependent on the dimensionless acceleration

$$\Gamma = \frac{A(2\pi f)^2}{g}, \tag{18}$$

where g is the gravitational acceleration and A and f are the fibers' amplitude and frequency of oscillation, respectively, which are plotted over a combination of the Reynolds number and the Laplace number multiplied by the ratio of the amplitude A and the fiber radius r_f, resulting in

$$\Pi_{df} = \frac{A}{r_f} Re_{r_d,air}\, La. \tag{19}$$

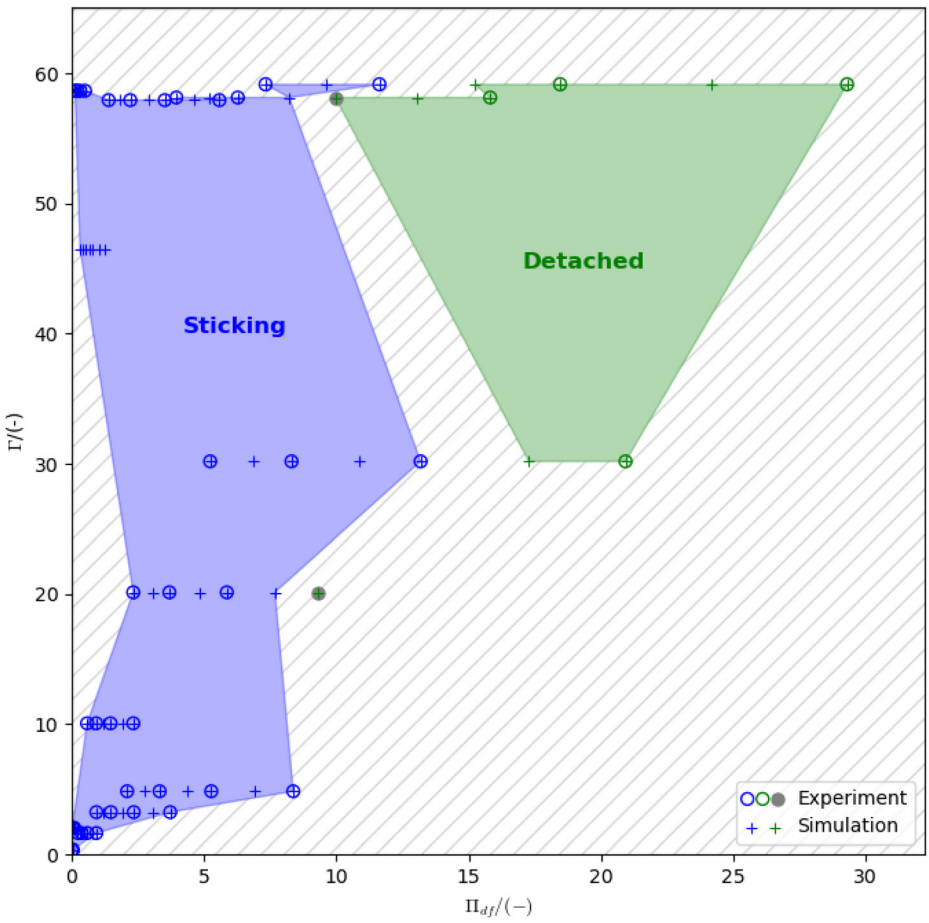

FIG. 19. Regime map sticking and detaching droplet.

The Laplace number *La*, the Reynolds number *Re*, and the Weber number *We* are defined as follows:

$$La = \frac{Re_{d,oil}^2}{We}, \tag{20}$$

$$Re_{d,air} = \frac{Afr_d}{\nu_{air}}, \tag{21}$$

$$Re_{d,oil} = \frac{Afr_d}{\nu_{oil}}, \tag{22}$$

$$We = \frac{\rho_{oil} r_d (Af)^2}{\sigma}, \tag{23}$$

where ν_{air} and ν_{oil} are the kinematic viscosity of the air and oil, respectively, and r_f is the radii of the fiber, and r_d is the sphere volume equivalent radius of the droplet [Eq. (11)]. The resulting dimensionless number Π_{df} is called the fiber-droplet-oscillation number and can be reduced to

$$\Pi_{df} = \frac{f\sigma r_d^2 A^2}{\nu_{air}\nu_{oil}\mu_{oil} r_f}, \tag{24}$$

with the dynamic viscosity of the oil μ_{oil} evaluating the ratio of inertial to viscous forces of oil and air additional to the droplets' surface tension scaled by the ratio of the oscillation amplitude to the fiber radius.

The regime map shows and summarizes the results of about 48 experiments, which were repeated at least two times, and 100 simulations and characterizes the droplet behavior with respect to sticking to the fiber and detaching. It is worth noting that the simulations were stopped after 0.5 s and that the results in most cases matched with those observed in the experiments. In two configurations, the experiments were not able to provide reproducible results (gray filled dots in Fig. 19). In those cases, the simulations suggested that the droplet detaches from the fiber, which was also the case in the majority of the experiments.

It is noteworthy that Poulain *et al.*,[11] who conducted experiments on water droplets applied to an excited fiber, utilize the Reynolds number

$$Re_\delta = \frac{2\pi f r_d^2}{\nu} = 2\left(\frac{r_d}{\delta}\right)^2 \tag{25}$$

with the ratio of the Stokes' boundary layer $\delta = (\nu/(\pi f))^{0.5}$ and the droplet's sphere equivalent radius r_d to estimate the influence of viscosity on the droplet. Because, in their case, $Re_\delta \gtrsim 100$, they conclude that the viscous effects are localized in a thin boundary layer, and the majority of the flow in the droplet is inertial.

In the presented work, $Re_\delta \lesssim 3$, indicating that viscous effects are prevalent throughout the flow in the entire droplet. The fiber-droplet-oscillation number Π_{df} can be expressed as a function of Re_δ:

$$\Pi_{df} = \frac{\sigma A^2}{\nu_{air}\mu_{oil} r_f}\frac{Re_\delta}{2\pi}, \tag{26}$$

yielding a disparity of two orders of magnitude in the fiber-droplet-oscillation number, rendering both cases challenging to compare.

VII. CONCLUSIONS

In this work, the fiber is observed from an axial direction during excitation for the first time, which enables information about the movement of the droplet in the circumferential direction at all times during the droplet–fiber interaction when vibration is acting radial to the fiber. Compared to the clam-shell-shaped droplets observed by Poulain *et al.*,[11] the here observed droplets are barrel shaped. Therefore, new motion patterns are identified. These are quasi-static, vertical oscillation, and reoccurring collapsing. Combinations of motion patterns lead to different mechanisms. The only motion pattern that cannot occur in combination with other motion patterns and, therefore, does not lead to a more complex mechanism is the quasi-static motion pattern. The motion patterns depend on the surface tension, the diameter of the droplet, the density and viscosity, and the amplitude and frequency of the external acceleration applied to the fiber. The characteristic mechanisms could be reproduced with a simplified two-dimensional simulation. Droplet detachment was observed for two mechanisms: first, when the droplet collapses repeatedly, and second, when vertical oscillations lead to an imbalance followed by a rotational motion with slinging and strong deformation.

The results suggest that the droplet detaches easier for higher Reynolds numbers and higher accelerations. Furthermore, the droplet tends to stick to the fiber for higher Weber numbers and smaller droplet volumes.

ACKNOWLEDGMENTS

We gratefully acknowledge that this project was funded by the Deutsche Forschungsgemeinschaft (DFG, German Research Foundation)—No. DFG/499469405.

AUTHOR DECLARATIONS

Conflict of Interest

The authors have no conflicts to disclose.

Author Contributions

A. Schwarzwaelder: Writing – original draft (equal). **F. Freese:** Writing – original draft (equal). **J. Meyer:** Supervision (equal). **K. Loganathan:** Data curation (equal). **H. Tietze:** Data curation (equal). **A. Dittler:** Supervision (equal). **U. Janoske:** Supervision (equal).

DATA AVAILABILITY

The data that support the findings of this study are available from the corresponding author upon reasonable request.

REFERENCES

[1]S. Michielsen and H. J. Lee, "Design of a superhydrophobic surface using woven structures," Langmuir **23**, 6004–6010 (2007).
[2]D. Chen, L. Tan, H. Liu, J. Hu, Y. Li, and F. Tang, "Fabricating superhydrophilic wool fabrics," Langmuir **26**, 4675–4679 (2010).
[3]C. Straube, J. Meyer, and A. Dittler, "Identification of deposited oil structures on thin porous oil mist filter media applying μ-CT imaging technique," Separations **8**, 193 (2021).
[4]S. Wurster, J. Meyer, H. E. Kolb, and G. Kasper, "Bubbling vs. blow-off—On the relevant mechanism(s) of drop entrainment from oil mist filter media," Sep. Purif. Technol. **152**, 70–79 (2015).
[5]N. M. Farhan and H. V. Tafreshi, "Using magnetic field to measure detachment force between a nonmagnetic droplet and fibers," Langmuir **35**(25), 8490–8499 (2019).
[6]R. Labbé and C. Duprat, "Capturing aerosol droplets with fibers," Soft Matter **15**, 6946–6951 (2019).
[7]M. Davoudi, M. M. Amrei, H. V. Tafreshi, and G. G. Chase, "Measurement of inflection angle and correlation of shape factor of barrel-shaped droplets on horizontal fibers," Sep. Purif. Technol. **204**, 127–132 (2018).
[8]X. Yang, X. Zhang, H. Wang, and G. G. Chase, "Vibration assisted water-diesel separation by electrospun PVDF-HFP fiber mats," Sep. Purif. Technol. **171**, 280–288 (2016).
[9]S. C. Kim, H. Wang, M. Imagawa, D.-R. Chen, and D. Y. H. Pui, "Experimental and modeling studies of the stream-wise filter vibration effect on the filtration efficiency," Aerosol Sci. Technol. **40**, 389–395 (2006).
[10]A. Bick, F. Boulogne, A. Sauret, and H. A. Stone, "Tunable transport of drops on a vibrating inclined fiber," Appl. Phys. Lett. **107**(18), 181604 (2015).
[11]S. Poulain and A. Carlson, "Sliding, vibrating swinging droplets an oscillating fibre," arXiv:2210.06314 (2022).
[12]N. M. Farhan, H. Aziz, and H. V. Tafreshi, "Simple method for measuring intrinsic contact angle of a fiber with liquids," Exp. Fluids **60**, 87 (2019).
[13]C. Hirt and B. Nichols, "Volume of fluid (VOF) method for the dynamics of free boundaries," J. Comput. Phys. **39**, 201–225 (1981).
[14]H. Rusche, "Computational fluid dynamics of dispersed two-phase flows at high phase fractions," Ph.D. thesis (Imperial College London, London, 2003).
[15]J. U. Brackbill, D. B. Kothe, and C. Zemach, "A continuum method for modeling surface tension," Technical Report (1992).
[16]E. Gauthier, T. Hellstern, I. G. Kevrekidis, and J. Benziger, "Drop detachment and motion on fuel cell electrode materials," ACS Appl. Mater. Interfaces **4**, 761–771 (2012).
[17]N. Ojaghlou, H. V. Tafreshi, D. Bratko, and A. Luzar, "Dynamical insights into the mechanism of a droplet detachment from a fiber," Soft Matter **14**, 8924–8934 (2018).
[18]N. M. Farhan and H. Vahedi Tafreshi, "Universal expression for droplet-fiber detachment force," J. Appl. Phys. **124**(7), 075301 (2018).